

A Bose-Einstein Condensate on a Synthetic Hall Cylinder

Chuan-Hsun Li,¹ Yangqian Yan,² Sayan Choudhury², David B. Blasing²,
Qi Zhou^{2,3,*}, and Yong P. Chen^{2,1,3,†}

¹School of Electrical and Computer Engineering, Purdue University,
West Lafayette, Indiana 47907, USA

²Department of Physics and Astronomy, Purdue University, West Lafayette, Indiana 47907, USA

³Purdue Quantum Center, Purdue University, West Lafayette, Indiana 47907, USA

*To whom correspondence should be addressed; E-mail: zhou753@purdue.edu

†To whom correspondence should be addressed; E-mail: yongchen@purdue.edu

Abstract

The geometry of a physical space is a key ingredient underlying many exotic quantum phenomena. However, accessing physical spaces with non-trivial geometries and many associated unique phenomena are often impeded by experimental constraints. Here, we realize a Bose-Einstein condensate (BEC) on a synthetic cylindrical surface subject to a net radial synthetic magnetic flux, topologically equivalent to a two-dimensional (2D) Hall ribbon with two edges connected. This cylindrical surface comprises a real spatial dimension and a curved synthetic dimension formed by cyclically-coupled spin states. The BEC on such a Hall cylinder has counterintuitive properties unattainable by its counterparts in 2D planes. It develops a crystalline order with a nonsymmorphic symmetry and the period of its density modulation halves the lattice spacing. Bloch oscillations of the BEC in the momentum space double the period of the band structure, analogous to traveling on a Mobiüs strip. Our work opens the door to engineering synthetic curved spaces and observing intriguing quantum phenomena inherent to the topology of spaces.

Spaces with nontrivial geometries play fundamentally important roles in many branches of physics such as general relativity and cosmology (1), photonics (2), and condensed matter physics (3). It is known that quantum systems in such spaces often exhibit counterintuitive prop-

erties difficult to attain in flat spaces. Superfluids on a cylindrical surface as well as some other curved manifolds carry vortices with no counterparts in 2D planes (4–6). Fractional quantum Hall states become degenerate on a torus, underlying the profound concept of topological order (7). Though novel quantum phenomena unique to spaces with non-trivial geometries have attracted longstanding theoretical interest since the birth of quantum mechanics, there have been limited experimental realizations due to technical challenges of fabricating such spaces and physical laws that further impose constraints. For instance, it is difficult to thread a net magnetic flux through the cylindrical surface of a nanotube. For a sphere and other closed surfaces, such a task is even impossible due to the lack of a magnetic monopole in nature.

The highly controllable laser-atom interactions have allowed bypassing the constraints in conventional systems possible and delivered a variety of synthetic topological matters (8–10), such as artificial magnetic monopoles (11, 12) and synthetic spin-orbit coupling for bosonic (13–17) and fermionic (18–21) gases. So far, most studies have been focusing on spaces with relatively simple geometries, for instances, Hall ribbons with open boundary conditions (22, 23) equivalent to 2D systems whose edges are disconnected. In our experiments, we produce a 3D ^{87}Rb BEC with a typical atom number $\sim 1 - 2 \times 10^4$ in an optical dipole trap. The BEC is then loaded to the cylindrical surface of a synthetic Hall cylinder by turning on a cyclic coupling among (hyperfine) spin states of the BEC, effectively delivering a periodic boundary condition in the synthetic dimension and connecting the two edges of a 2D Hall ribbon.

As shown in Fig. 1AB, four spin states, $|F, m_F\rangle = |2, 2\rangle, |2, 1\rangle, |1, 0\rangle, |1, 1\rangle$ relabeled as $|1\rangle, |2\rangle, |3\rangle, |4\rangle$, form discrete sites in the synthetic dimension (24) referred to the w direction. Utilizing $F = 1$ and $F = 2$ (hyperfine) manifolds makes a cyclic coupling in the w direction possible, since a transition of $\Delta m_F = \pm 2$ is extremely weak in the $F = 1$ manifold of alkali atoms (25). Counter-propagating Raman lasers along \hat{y} , with an angular frequency difference $\Delta\omega_R$ and a coupling strength Ω , couple $|1\rangle$ and $|2\rangle$ as well as $|3\rangle$ and $|4\rangle$. The Raman laser at

the magic wavelength $\lambda \sim 790$ nm (26) sets the photon recoil momentum $\hbar k_r = 2\pi\hbar/\lambda$ and recoil energy $E_r = \hbar^2 k_r^2/(2m)$, where \hbar is the reduced Planck constant and m is the atomic mass of ^{87}Rb . Two microwave fields, with coupling strengths Ω_1 and Ω_2 , couple respectively $|2\rangle$ and $|3\rangle$, and $|1\rangle$ and $|4\rangle$. The combination of these Raman and microwave fields delivers a cyclic coupling, effectively a closed circle, in the w direction. Thus, our scheme synthesizes the y and the curved w dimensions into a cylindrical surface, schematized in Fig. 1C.

An atom obtains a net momentum of $\hbar K$ along \hat{y} from a Raman transition, thus acquiring a quantum mechanical y -dependent phase factor, e^{iKy} (27), where $K = 2k_r$. Such a phase has been used to engineer an artificial magnetic flux (22–24). Since the Raman-induced momentum transfer is along \hat{y} and the x and z -directions are decoupled from the cylindrical surface, the single-particle Hamiltonian describing the light-matter couplings in Fig. 1B and the atomic motions along \hat{y} can be written in the basis of $\{|1\rangle, |2\rangle, |3\rangle, |4\rangle\}$ as (27)

$$H = \frac{\hat{p}_y^2}{2m} \mathbf{I} + \begin{pmatrix} -\delta_R & \frac{\Omega}{2}e^{iKy} & 0 & \frac{\Omega_2}{2} \\ \frac{\Omega^*}{2}e^{-iKy} & \varepsilon_0 & \frac{\Omega_1}{2} & 0 \\ 0 & \frac{\Omega^*}{2} & \varepsilon_0 & \frac{\Omega}{2}e^{iKy} \\ \frac{\Omega_2^*}{2} & 0 & \frac{\Omega^*}{2}e^{-iKy} & \delta_R \end{pmatrix}, \quad (1)$$

where $\hat{p}_y = -i\hbar\frac{\partial}{\partial y}$ is the momentum operator along \hat{y} , \mathbf{I} is the identity matrix, the detuning δ_R is zero in this work, ε_0 is the quadratic Zeeman shift. H has four unique features. First, the Raman-induced y -dependent phase factor, e^{iKy} , cannot be gauged away due to the implemented periodic boundary condition, unlike open boundary conditions such as $\Omega_2 = 0$. This makes H periodic in y , corresponding to an underlying real-space lattice with a period of $d \equiv 2\pi/K = \pi/k_r$. Second, a total y -dependent phase factor e^{i2Ky} accumulated after an atom completes a cycle clockwise along \hat{w} implies a net magnetic flux penetrating the cylindrical surface. As shown in Fig. 1C, a magnetic flux $\Phi/\Phi_0 = -Kd/(2\pi)$ per shaded lattice plaquette of area of d times one unit length along \hat{w} is indicated by a thick yellow arrow, where $\Phi_0 = 2\pi\hbar/q$ is the magnetic flux quantum and $q \equiv -1$ is the effective charge of a particle. Third, a BEC on

such a synthetic Hall cylinder described by H develops a crystalline order in its density along \hat{y} (Fig. 1C). As explained later, this density modulation has a period of $d/2$ (half period of the lattice and H) due to the underlying nonsymmorphic symmetry. We emphasize that unlike previous works using real-space external optical lattices (22–24), here the emergent crystalline order of atomic density is purely a result of “curving” a planar space to a cylinder. As shown later, the crystalline order vanishes on an “unzipped” cylinder when imposing an open boundary condition along \hat{w} by turning off Ω_2 . Fourth, whereas the period of H is d , H is invariant under a translation of $d/2$ along \hat{y} followed by a unitary transformation along \hat{w} given by $|1\rangle \rightarrow |1\rangle$, $|2\rangle \rightarrow -|2\rangle$, $|3\rangle \rightarrow -|3\rangle$, $|4\rangle \rightarrow |4\rangle$. Such a nonsymmorphic symmetry (27) is of great interest because it can lead to symmetry-protected band crossings (9), which can play an important role in topological quantum matters such as topological semimetals (28). Because of the band crossings, unconventional Bloch oscillations that mimic the transport on a Mobiüs strip can arise (9, 29, 30).

The emergent lattice and BEC density modulation can also be understood in the momentum space. Fig. 2A illustrates light-induced couplings between the BEC wavefunction’s constituent plane waves, each characterized by a given spin state and mechanical momentum along \hat{y} . Our cyclic coupling leads to two independent branches in the momentum-spin space, $H_1(q_y)$ and $H_2(q_y)$ represented by line-connected solid/dashed circles, where $\hbar q_y$ is the quasimomentum, $\hbar k_y = \hbar(q_y \pm nK)$ is the mechanical momentum, and n is an integer. On one hand, each branch satisfies $H_{i=1,2}(q_y) = H_{i=1,2}(q_y + n \times 2K)$, corresponding to a sublattice with a period of $d' = 2\pi/(2K) = d/2$ and thus the $d/2$ periodicity of the associated density modulation. On the other hand, these two branches are offset from each other by $\hbar K$. Thus, the energy spectrum $E(q_y)$ consists of two sets of bands, $E_1(q_y)$ and $E_2(q_y)$ that satisfy $E_1(q_y) = E_2(q_y + K)$. These two sets of bands intersect at the boundary of the Brillouin zone, $q_y = \pm\pi/d = \pm K/2$, when $E(q_y) = E(-q_y)$ is satisfied (27). For a BEC at $q_y = 0$ in the ground band of Fig. 2B, the phase

of each spin state's wavefunction has a periodicity of either d or $d' = d/2$ (27), as indicated in Fig. 1C by the + and – signs respectively representing a phase of 0 and π at the positions (y) of maximum densities. Therefore, the phase of the total wavefunction of the BEC has a periodicity of d , consistent with the size ($2\pi/d$) of the Brillouin zone.

To probe the density's crystalline order with a nonsymmorphic symmetry, we perform spin-revolved quantum transport measurements, using Bloch oscillations of a BEC initially prepared (27) at $q_y = 0$ in either band 1 or band 2 in the first Brillouin zone (Fig. 2B). Subsequently, the dipole trap is abruptly turned off at $t_{hold} = 0$, allowing the atoms to fall under the gravity (towards $-\hat{y}$, Fig. 1A) for various time t_{hold} , during which the coupling fields remain at the final values. Such a procedure for quantum transport measurement, by turning off the trap abruptly while keeping the relevant coupling fields for various t_{hold} , is used for all experiments presented later. The gravitational force renders the transport of the BEC towards negative q_y in the band structure, inducing BEC's Bloch oscillations due to the presence of the periodic band structure. During Bloch oscillations, the total mechanical momentum along \hat{y} of the BEC, $\hbar k_{BEC}$, directly probes the slope of the Bloch band (or the group velocity v_p of the BEC) as a function of t_{hold} or q_y based on $\frac{\hbar k_{BEC}(q_y)}{m} = v_p(q_y) = \frac{1}{\hbar} \frac{dE(q_y)}{dq_y}$ (31), where E is the eigenenergy. Both v_p and E are functions of q_y , where $q_y = q_0 + F_g t_{hold}/\hbar$ is a function of t_{hold} , F_g is the gravitational force, and in our case the initial quasimomentum $\hbar q_0 = 0$. After various t_{hold} , we immediately turn off all the coupling fields to release the atoms for a 15-ms time-of-flight (TOF) including a 9-ms spin-resolved Stern-Gerlach process, and then perform absorption imaging. These TOF images reveal the spin and mechanical momentum compositions of a BEC at various t_{hold} and the corresponding q_y . We obtain $\hbar k_{BEC}$ by summing over population-weighted mechanical momentum components along \hat{y} (27). The q_y -dependent spin compositions of the BEC directly probe the spin texture of the Bloch band. The quasimomentum of the BEC at t_{hold} can be measured (27) by the displacement of the mechanical momentum components of, say $|1\rangle$ and $|4\rangle$, at

t_{hold} relative to their mechanical momentum components at $t_{hold} = 0$ ($q_y = 0$).

TOF images obtained for the initial preparations in either band 1 or band 2 are shown respectively in Fig. 2C and Fig. 2D, with their corresponding analyzed data (dots) labeled by either band 1 or band 2. The total mechanical momentum ($\hbar k_{BEC}$) versus t_{hold} and versus quasimomentum are respectively shown in Fig. 2E and Fig. 2F. The fractional spin populations of $|1\rangle$ plus $|4\rangle$, and $|2\rangle$ plus $|3\rangle$, versus t_{hold} are shown in Fig. 2GH. Two notable features are discussed. First, we observe in Fig. 2CD that spin and momentum compositions of the BEC repeatedly show up with a period of $2\hbar K$ in quasimomentum (or a period of ~ 2.6 ms in time), twice the $\hbar K$ periodicity of the band structure (Fig. 2B). Such a double periodicity is also observed in Fig. 2F, which demonstrates the $2\hbar K$ periodicity of Bloch oscillations in quasimomentum. This transport behavior is analogous to traveling on a Möbius strip: atoms have to travel twice the period of the band structure to reach the same quantum state (up to a phase). According to the momentum-position duality, the observed $2\hbar K$ periodicity (twice the period of the band structure) of Bloch oscillations is consistent with the calculated $d/2$ periodicity (half the period of the lattice described by H) of the real-space densities illustrated in Fig. 1C. Note that the q_y in Fig. 2F is plotted modulo $2K$ (i.e., q_y is equivalent to $q_y \pm n \times 2K$), only between $-K$ and K for both band 1 and band 2 due to their $2K$ periodicity in q_y . This $2\hbar K$ periodicity is also reflected by the observation of the $2\hbar K$ separation between different mechanical momentum components for each spin state in Fig. 2CD. Second, we observe that the spin and mechanical momentum composition of the BEC at a given t_{hold} or q_y in Fig. 2C can be found in Fig. 2D with an offset by ~ 1.3 ms or $\sim K$. Such an offset in t_{hold} or q_y is also respectively observed in Fig. 2EGH and Fig. 2F, where data of band 1 and band 2 exhibit out-of-phase Bloch oscillations in t_{hold} or q_y . These observed out-of-phase Bloch oscillations with a double period of the band structure is consistent with the feature of band crossings: atoms traveling to the band touching points would undergo a perfect (diabatic) transition from the ground band to the first excited band because

of the vanishing band gap (32), unlike conventional Landau-Zener tunnelings with a finite band gap (16).

Therefore, during Bloch oscillations, if we regard the trajectory of the BEC in the momentum space as one band, band 1 and band 2 between $q_y = -1.5K$ ($1.5K$) and $-0.5K$ ($0.5K$) become respectively the first excited and the ground bands as labeled in Fig. 2B. Consequently, both bands have a periodicity of $2\hbar K$, doubling the reciprocal lattice vector $\hbar K$, and are exactly the same but shifted from each other by $\hbar K$, thus giving rise to band crossings occurring with a period of $\hbar K$. This is another manifestation of the nonsymmorphic symmetry discussed above. Further, since Bloch oscillations can be used to map out (33) the band structure, Fig. 2F can directly reveal the lowest two crossing bands in Fig. 2B. In Fig. 2E-H, the experimental data are in agreement with theoretical calculations (solid lines) (27) using the same parameters as used in Fig. 2B provided the average of the measured $d(\hbar q_y)/d(t_{hold})$ (27).

These nonsymmorphic symmetry-protected band crossings remain under any perturbations respecting the symmetry, such as variations of parameters in equation (1). Thus, the demonstrated “momentum-space Mobiüs strip” is protected by the nonsymmorphic symmetry. It is then interesting to introduce perturbations that break the nonsymmorphic symmetry and probe the resulting changes in the band structure by Bloch oscillations. As shown in Fig. 3A, the nonsymmorphic symmetry can be broken by applying a radio frequency (RF) wave (with an angular frequency of $\Delta\omega_R$) to couple $|1\rangle$ and $|2\rangle$ as well as $|3\rangle$ and $|4\rangle$, in addition to the Raman and microwave couplings. This results in a new Hamiltonian, H' (27), which is no longer invariant under the nonsymmorphic symmetry. Nevertheless, both H and H' still have the same periodicity of $d = 2\pi/K$ in the real space and $\hbar K$ in the momentum space. However, the two branches (each has a period of $2\hbar K$) in Fig. 2A merge into one that has a period of $\hbar K$, giving rise to a new band structure (Fig. 3C) that has band gap opening at the crossing points observed in Fig. 2B. We probe this new periodic band structure by performing the quantum transport

measurement using the same procedure. Fig. 3D presents TOF images at various t_{hold} and the corresponding q_y , with the analyzed data (dots) for the total mechanical momentum versus t_{hold} and quasimomentum respectively shown in Fig. 3EF. As shown in Fig. 3D-F, the oscillations of BEC's spin and mechanical momentum composition and the total momentum have a period of ~ 1.3 ms or $\hbar K$, half the period as those observed in Fig. 2. The $\hbar K$ periodicity is now identical to the period of the lattice and H' , suggesting that q_y becomes equivalent to $q_y \pm nK$. This $\hbar K$ periodicity is also reflected by the observation of the $\hbar K$ separation between different mechanical momentum components for each spin state in Fig. 3D. Based on the observed dynamics, the symmetry-breaking perturbation has effectively “untwisted” the momentum-space Mobiüs strip into a regular one.

Lastly, we demonstrate that unzipping the cyclic coupling turns the cylindrical surface into a planar 2D ribbon, where the emergent lattice, BEC density modulation, and Bloch oscillations disappear. Theoretically, this is because when removing one segment of the cyclic coupling and effectively imposing an open boundary condition in the w direction, for instance, by setting $\Omega_2 = 0$ (Fig. 4A), the Raman-imprinted phase factor e^{iK_y} in equation (1) can be gauged away. In our experiments, we keep couplings Ω and Ω_1 but remove Ω_2 in Fig. 1B, using the same parameters as used in Fig. 2B except $\Omega_2 = 0$. This results in a single-particle dispersion shown in Fig. 4B, which we probe by performing the similar quantum transport measurement for a BEC initially prepared at the minimum of the right well ($q_y \approx K$). Fig. 4C presents TOF images at various t_{hold} and the corresponding q_y , with analyzed data (dots) for the total mechanical momentum versus t_{hold} shown in Fig. 4D and fractional spin populations versus t_{hold} shown in Fig. 4E. Data in Fig. 4C-E do not exhibit a periodicity, consistent with the observation of only one mechanical momentum component for each spin state in TOF images. These observations are consistent with the theoretical calculations (solid lines in Fig. 4DE) using the same parameters as used in Fig. 4B. Because the dispersion relation is not a periodic band structure like

those in Fig. 2B and Fig. 3C, $\hbar k_{\text{BEC}}$ eventually keeps increasing due to the gravity. The spin composition of the BEC is initially dominated by $|4\rangle$ but becomes dominated by $|1\rangle$ at later times, consistent with the calculated spin texture of the dispersion relation.

Synthetic spaces are highly controllable and able to lift many constraints in real spaces. A BEC on a synthetic cylindrical surface has allowed us to access quantum phenomena absent in planar 2D spaces. Our work paves the way for future theoretical and experimental efforts of engineering the geometry and topology of a broader range of synthetic spaces, including curved spaces, to explore unprecedented quantum phenomena.

References and Notes

1. S. M. Carroll, *Spacetime and geometry: An introduction to general relativity* (2004).
2. N. Schine, A. Ryou, A. Gromov, A. Sommer, J. Simon, *Nature* **534**, 671 (2016).
3. H. Kleinert, *Gauge Fields in Condensed Matter* (WORLD SCIENTIFIC, 1989).
4. A. M. Turner, V. Vitelli, D. R. Nelson, *Rev. Mod. Phys.* **82**, 1301 (2010).
5. T.-L. Ho, B. Huang, *Phys. Rev. Lett.* **115**, 155304 (2015).
6. N.-E. Guenther, P. Massignan, A. L. Fetter, *Phys. Rev. A* **96**, 063608 (2017).
7. X. G. Wen, Q. Niu, *Phys. Rev. B* **41**, 9377 (1990).
8. N. Goldman, J. C. Budich, P. Zoller, *Nature Physics* **12**, 639 (2016).
9. S.-L. Zhang, Q. Zhou, *Journal of Physics B: Atomic, Molecular and Optical Physics* **50**, 222001 (2017).
10. O. Boada, A. Celi, J. Rodrguez-Laguna, J. I. Latorre, M. Lewenstein, *New Journal of Physics* **17**, 045007 (2015).

11. M. W. Ray, E. Ruokokoski, S. Kandel, M. Möttönen, D. S. Hall, *Nature* **505**, 657 (2014).
12. S. Sugawa, F. Salces-Carcoba, A. R. Perry, Y. Yue, I. B. Spielman, *Science* **360**, 1429 (2018).
13. Y.-J. Lin, K. Jiménez-García, I. B. Spielman, *Nature* **471**, 83 (2011).
14. J.-Y. Zhang, *et al.*, *Phys. Rev. Lett.* **109**, 115301 (2012).
15. C. Qu, C. Hamner, M. Gong, C. Zhang, P. Engels, *Phys. Rev. A* **88**, 021604 (2013).
16. A. J. Olson, *et al.*, *Phys. Rev. A* **90**, 013616 (2014).
17. Z. Wu, *et al.*, *Science* **354**, 83 (2016).
18. P. Wang, *et al.*, *Phys. Rev. Lett.* **109**, 095301 (2012).
19. L. W. Cheuk, *et al.*, *Phys. Rev. Lett.* **109**, 095302 (2012).
20. L. Huang, *et al.*, *Nature Physics* **12**, 540 (2016).
21. S. Kolkowitz, *et al.*, *Nature* **542**, 66 (2017).
22. B. K. Stuhl, H.-I. Lu, L. M. Aycock, D. Genkina, I. B. Spielman, *Science* **349**, 1514 (2015).
23. M. Mancini, *et al.*, *Science* **349**, 1510 (2015).
24. A. Celi, *et al.*, *Phys. Rev. Lett.* **112**, 043001 (2014).
25. I. H. Deutsch, P. S. Jessen, *Optics Communications* **283**, 681 (2010).
26. L. J. LeBlanc, J. H. Thywissen, *Phys. Rev. A* **75**, 053612 (2007).
27. Materials and methods are available as supplementary materials.

28. A. A. Burkov, *Nature Materials* **15**, 1145 (2016).
29. K. Shiozaki, M. Sato, K. Gomi, *Phys. Rev. B* **91**, 155120 (2015).
30. Q.-Z. Wang, C.-X. Liu, *Phys. Rev. B* **93**, 020505 (2016).
31. M. Ben Dahan, E. Peik, J. Reichel, Y. Castin, C. Salomon, *Phys. Rev. Lett.* **76**, 4508 (1996).
32. S.-L. Zhang, Q. Zhou, *Phys. Rev. A* **95**, 061601 (2017).
33. E. Peik, M. Ben Dahan, I. Bouchoule, Y. Castin, C. Salomon, *Phys. Rev. A* **55**, 2989 (1997).

Acknowledgements

Our experiment has been supported by NSF grant PHY-1708134. D. B. B. also acknowledges support by the Purdue Research Foundation Ph.D. fellowship. Q. Z. acknowledges startup funds from Purdue.

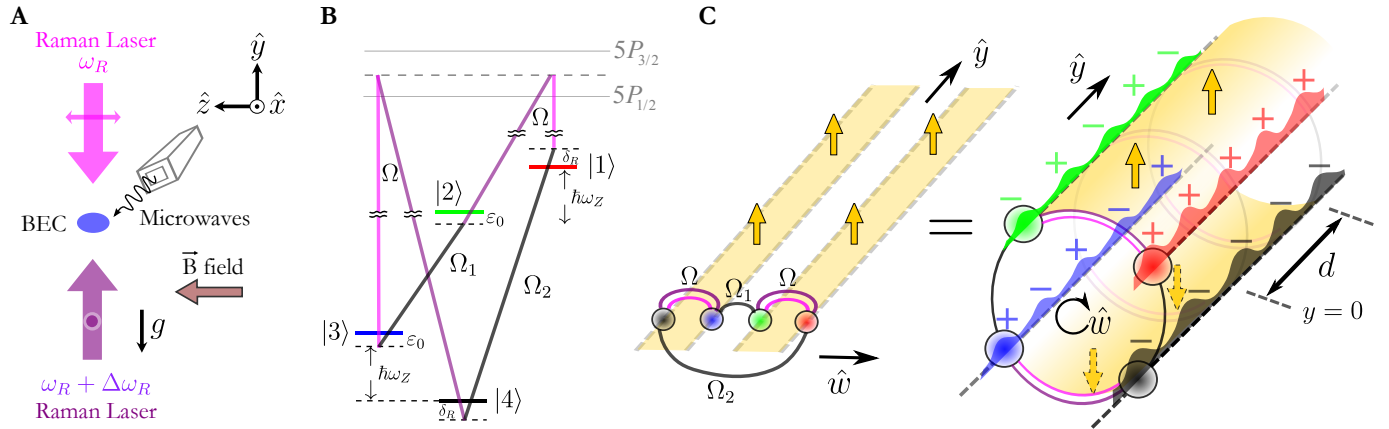


Figure 1: Experimental setup for realizing a synthetic Hall cylinder. (A-B) Raman lasers with orthogonal linear polarizations (A, double-headed arrows) counter-propagate along \hat{y} . Gravity “ g ” is towards $-\hat{y}$. Hyperfine spin states (B, indicated by different colors) $|1\rangle$ and $|2\rangle$, and $|3\rangle$ and $|4\rangle$ are Raman coupled with strength Ω . Linear Zeeman splitting $\hbar\omega_Z \approx \hbar\Delta\omega_R \approx \hbar \times (3.5 \text{ MHz})$ is generated by a bias magnetic field $\vec{B} = B\hat{z}$, which sets the detuning $\delta_R = \hbar(\Delta\omega_R - \omega_Z) = 0$. The quadratic Zeeman shift $\varepsilon_0 \approx 2.4 E_r$. Microwaves (frequency $\approx 6.8 \text{ GHz}$, from a microwave horn) propagating in the $x - y$ plane couple $|2\rangle$ and $|3\rangle$, and $|1\rangle$ and $|4\rangle$, with respective strengths $\Omega_{1,2}$. Four spin states as discrete sites are cyclically-coupled (a periodic boundary condition) to form a closed circle in the synthetic dimension \hat{w} . (C) A Hall ribbon (left) in the 2D plane with two connected edges along \hat{w} is topologically equivalent to a cylindrical surface (right) subject to a radial magnetic flux (thick yellow arrows) generated by the Raman coupling. The emergent crystalline order of the BEC density has a periodicity of $d/2$, half period of the lattice and the Hamiltonian H . For a BEC at $q_y = 0$ in the ground band of Fig. 2B, the wavefunction’s phase (indicated by + and -) of each spin component has a periodicity of either d or $d/2$, leading to a d periodicity in the BEC wavefunction.

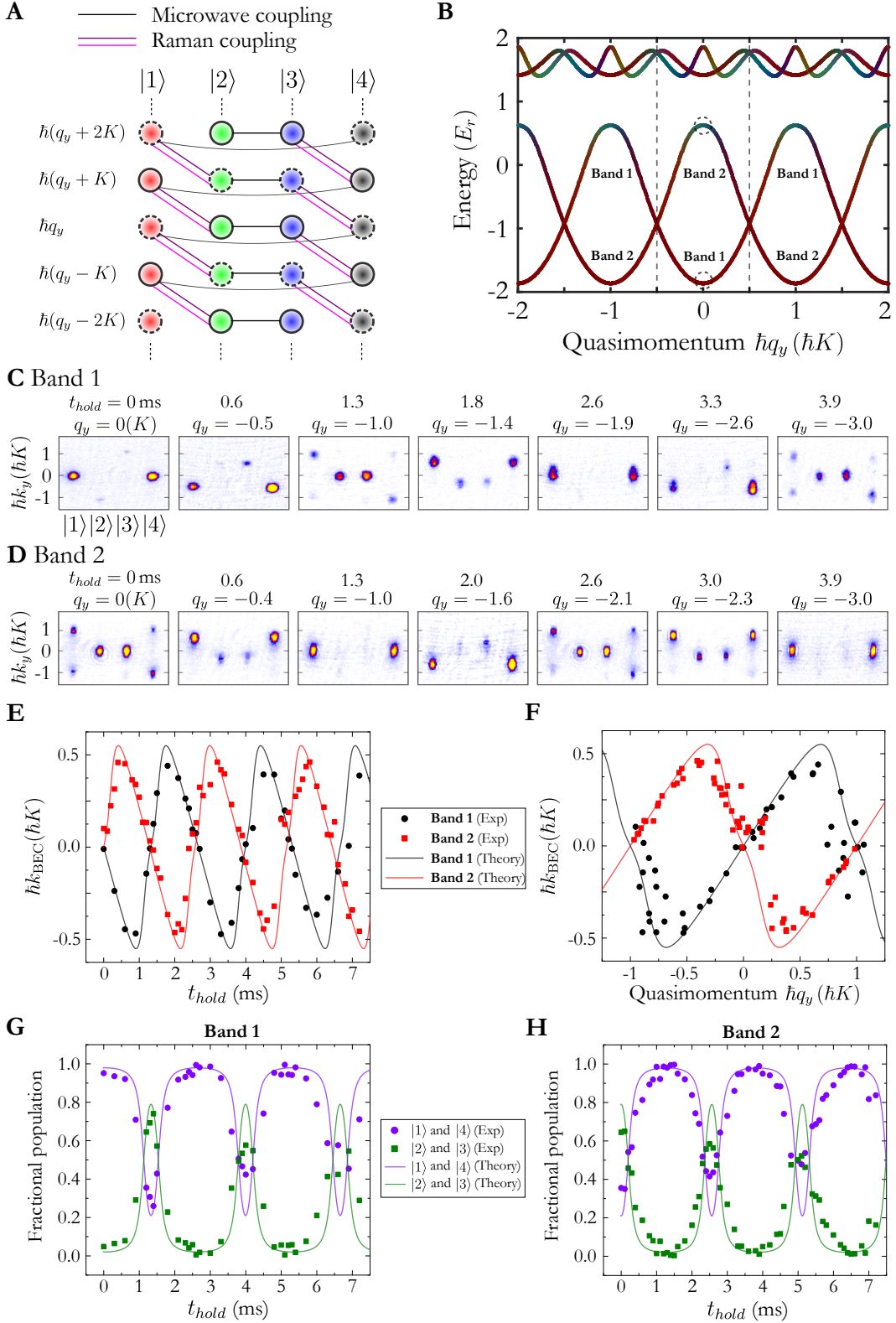


Figure 2: Band structure with a nonsymmorphic symmetry and observed Bloch oscillations. (A) Light-induced couplings between spin and mechanical momentum states. The cyclic coupling leads to an infinite number of mechanical momentum components $\hbar(q_y \pm nK)$ along \hat{y} . The underlying nonsymmorphic symmetry is manifested in the two independent branches (marked by solid/dashed circles) offset from each other by $\hbar K$. (B) Calculated band structure using $\Omega = 2.3$, $\Omega_1 = 2.5$, $\Omega_2 = 3.4$, $\delta_R = 0$, and $\varepsilon_0 = 2.4$, all in units of E_r . The spin texture is revealed by colors determined by the population-weighted colors of the four spin states (27). The first Brillouin zone is between the dashed lines. The BEC initially prepared at $\hbar q_y = 0$ (dashed circles) in either band 1 or band 2 undergoes gravity-induced transport and Bloch oscillations for various t_{hold} . (C-D) TOF images showing spin and mechanical momentum compositions of atoms taken at various t_{hold} and the corresponding q_y , respectively corresponding to the initial preparation in band 1 and band 2. Each TOF image (and the associated analyzed quantities presented later) is typically an average of a few repetitive measurements. (E-F) Total mechanical momentum of the BEC versus t_{hold} and quasimomentum, respectively. (G-H) Fractional spin populations versus t_{hold} .

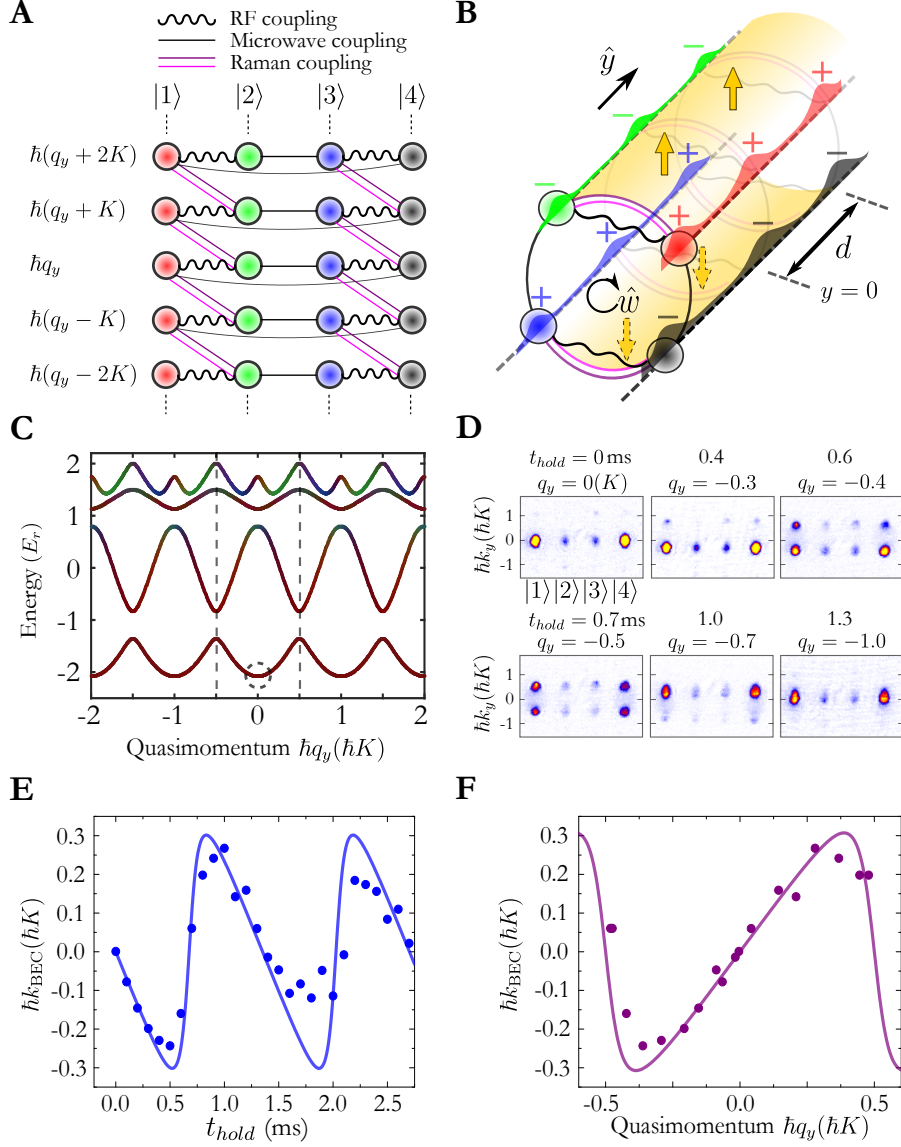


Figure 3: Breaking the nonsymmorphic symmetry and observed Bloch oscillations. (A) RF coupling (wiggling lines) merges the two independent branches in Fig. 2B, breaking the nonsymmorphic symmetry. (B) A cylinder with a broken nonsymmorphic symmetry, described by the Hamiltonian H' . For a BEC prepared at $q_y = 0$ in the ground band in (C), both the wavefunction's phase (indicated by + and -) and the crystalline order of the density have a periodicity of d , identical to the period of the lattice or the Hamiltonian H' . (C) Calculated band structure using the same parameters as used in Fig. 2B with the addition of $\Omega_{RF} = 1.6 E_r$. (D) TOF images at various t_{hold} for Bloch oscillations of a BEC starting from $q_y = 0$ (dashed circle in (C)). (E-F) Total mechanical momentum of the BEC versus t_{hold} and quasimomentum, respectively. The measured Bloch oscillations exhibit a periodicity of $\hbar K$ rather than the $2\hbar K$ observed in Fig. 2. Data in (F) correspond to the data in the first 1.5 ms in (E) before the Bloch oscillations exhibit notable damping.

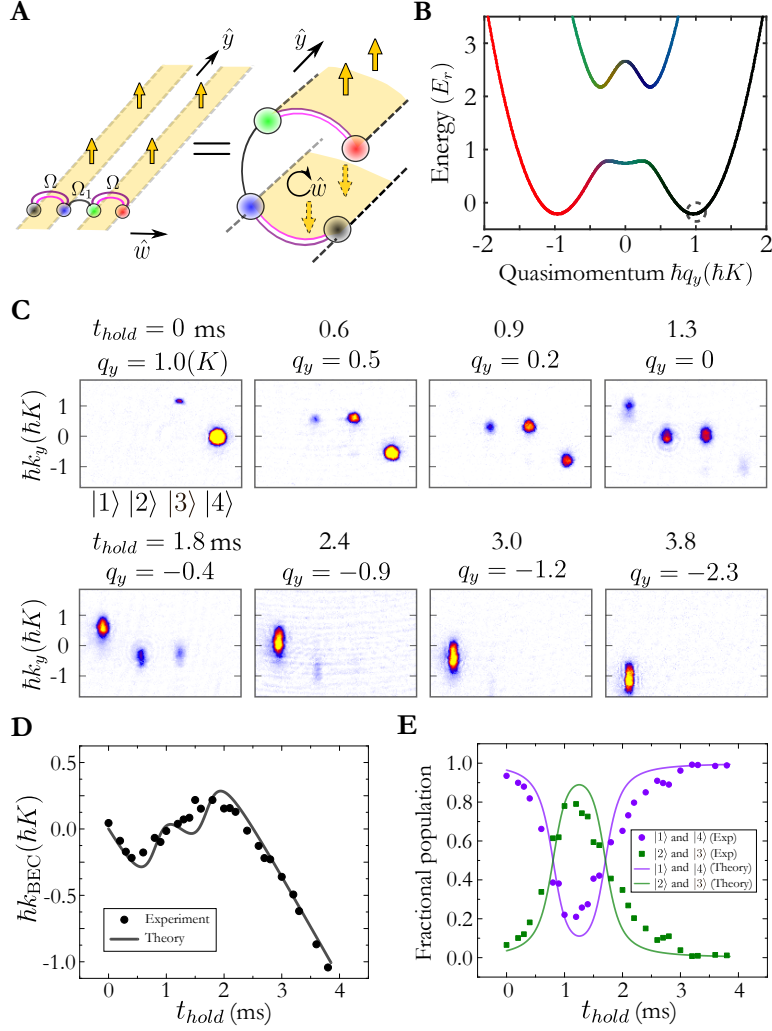


Figure 4: Unzipping the cylinder by cutting the cyclic coupling. (A) The unzipped Hall cylinder is topologically equivalent to a 2D planar Hall ribbon. (B) Dispersion relation calculated for $\Omega_2 = 0$, while keeping the other parameters the same as used in Fig. 2B. The BEC is initially prepared at the minimum of the right well ($q_y \approx K$, marked by the dashed circle). (C) TOF images at various t_{hold} and the corresponding quasimomentum for a BEC traveling towards negative q_y in the lowest band. (D) Total mechanical momentum of the BEC versus t_{hold} . (E) Fractional spin populations versus t_{hold} .